Realization of two-dimensional ferromagnetism with giant coercivity in ultrathin β-Ni(OH)$_2$ layers grown on a MoS$_2$ surface

Shatabda Bhattacharya,[1] Diptiman Dinda,[1] Bikash Kumar Shaw,[1] Saurav Dutta,[2] and Shyamal K. Saha[1,*]
[1]*Department of Materials Science, Indian Association for the Cultivation of Science, Jadavpur, Kolkata-700032, India*
[2]*Department of Physics, Rammohan College, University of Calcutta, Kolkata-700009, India*
(Received 28 October 2015; revised manuscript received 1 April 2016; published 4 May 2016)

Due to the charge transfer effect at the contact of transition metal (TM) and MoS$_2$, the use of ferromagnets in MoS$_2$ based spin transistor is not suitable. On the other hand, β-Ni(OH)$_2$ is known to be a layered type material with antiparallel Ni spins in alternate layers. Here, an ultrathin layer of antiferromagnetic β-Ni(OH)$_2$ is grown on the MoS$_2$ surface to achieve complete ferromagnetism with giant coercivity (2925 Oe). The origin of this ferromagnetic ordering is the reduction of Ni spin moments in Ni(OH)$_2$ layer adjacent to MoS$_2$ surface due to charge transfer from S to Ni. The use of antiferromagnetic layered type material to achieve ferromagnetic ordering with giant coercivity is a new concept to realize perfect two-dimensional (2D) ferromagnets which have major advantages due to the huge change in coercivity with thickness.

DOI: 10.1103/PhysRevB.93.184403

I. INTRODUCTION

Since the discovery of graphene, tremendous interests have grown concerning two-dimensional (2D) materials due to their potential applications in next generation nanoelectronic and spintronic devices [1–6]. To overcome the limitation of zero band gap property in graphene, molybdenum disulfide (MoS$_2$) has emerged as a potential alternative for 2D-based nanoelectronic and optoelectronic applications [7–9]. Although, intensive research on MoS$_2$ based field effect transistors has been carried out during the last few years, comparatively its use has been limited in spintronic devices in spite of having superior spin coherence length. The main reason behind this is the generation of Schottky barrier due to charge transfer at the MoS$_2$/ferromagnetic (Fe, Co, Ni) contacts [10–12]. This charge transfer effect, which is detrimental to spin transport, is also observed in graphene/transition metal (TM) interface [13–15]. Therefore, application of MoS$_2$ in spintronic devices using TM based contacts (Fe, Co, Ni, etc.) is limited. To overcome the limitation of the charge transfer effect at the MoS$_2$/TM interface, we have introduced a new concept to use layered type antiferromagnetic material instead of ferromagnetic layer on MoS$_2$ which will be useful in spintronic devices. The advantage of using this antiferromagnetic layered type material is the observation of ferromagnetic ordering with giant coercivity. Due to this charge transfer effect, spin moment of the layer adjacent to MoS$_2$ reduces, resulting in net uncompensated spins in the immediate upper layer. In addition to that, the use of this material provides an extra advantage in which the coercivity can be tuned in a wide range just by controlling the thickness of the antiferromagnetic layer.

In spin transistors with conventional ferromagnetic metals, switching fields at two different contacts is controlled by tuning the shape and size of the contacts. Hence, a wide variation of switching field is difficult to achieve [15–18]. However, in the present technique, switching fields at two different contacts can be varied easily by changing the thickness of the antiferromagnetic layer grown on MoS$_2$ surface. To establish this concept of achieving ferromagnetism with a wide range of coercivity, in the present paper, we have grown an ultrathin layer of β-Ni(OH)$_2$ considering MoS$_2$ as a template/surface.

β-Ni(OH)$_2$ is known to be an antiferromagnetic material with low coercivity (250 Oe) in its bulk phase [19–21]. In contrast, ferromagnetism with magnetic saturation and remarkably high coercivity ($\sim$2925 Oe) is achieved for our thin layered sample containing the lowest concentration of Ni precursor. Giant coercivity is achieved due to surface pinning of Ni^{2+} spins at the interface. The anomalous increase in magnetoconductivity with temperature is explained by the temperature dependent Rashba spin-orbit coupling [22–25] which decreases with increasing temperature.

II. SYNTHESIS AND STRUCTURAL CHARACTERIZATION

In the first step, the Ni(OH)$_2$ layer is grown on the MoS$_2$ surface with three different Ni concentrations, and the samples are designated as low concentration (LC), medium concentration (MC), and high concentration (HC), respectively. Concentration of the nickel precursor determines the thickness of Ni(OH)$_2$ layers grown on MoS$_2$ surface. For lowest Ni concentration, the thinnest Ni(OH)$_2$ layer was formed, i.e., sample LC. This is a very effective technique to tune the thickness of the nickel hydroxide layer just tuning the concentration of precursor. To synthesize 2D, Molybdenum sulfide sheets, 310 mg of hexaammonium heptamolybdate tetrahydrate (5 mmol) and 267 mg of thiourea (70 mmol) were dissolved in 35 ml of deionized water under vigorous stirring to form a homogeneous solution. Then, the solution was transferred into a 50 ml Teflon-lined stainless steel autoclave and maintained at 200 °C for 24 h. The resultant product was washed with water and absolute ethanol several times to remove all unreacted molecules/ions. Finally, the as synthesized MoS$_2$ was dried at 60 °C under vacuum. In the second step, to prepare a thin layer of Ni(OH)$_2$ on the MoS$_2$ surface, 50 mg of as synthesized MoS$_2$ powder was

*cnssks@iacs.res.in

dissolved into 100 ml of anhydrous DMF solution followed by ultrasonication treatment for 1 h. The solution was then heated slowly in a round bottom flask with magnetic stirring to reach the temperature at 80 °C. At this temperature, $Ni(Ac)_2$ was added into the solution, and the mixture was kept at 80 °C with stirring for 1 h. The as-synthesized composite was collected using centrifuge and washed with distilled water. The collected residue was again dispersed in 50 ml of water. The suspension was then sealed in a 50 ml Teflon lined stainless steel autoclave for hydrothermal reaction at 180 °C for 10 h. The final product was washed with water and ethanol repeatedly. The final product was dried in a vacuum oven at 60 °C to get $MoS_2/Ni(OH)_2$ composite powder. Three samples with different Ni-acetate concentrations designated as LC (5 mM), MC (12.5 mM), and HC (50 mM) were synthesized. Out of the three samples prepared, we have presented the results of MC and LC only. For HC, the thickness of $Ni(OH)_2$ layer was very high compared to other cases. Hence, the results obtained for HC were similar to those for the bulk phase, which have been omitted.

A. X-ray diffraction Rietveld and transmission electron microscopy analysis

Powder x-ray diffraction (XRD) measurements were carried out using powdered samples with an x-ray diffractometer (RICH SEIFERT-XRD 3000P having X-Ray Generator-Cu, 10 kV, 10 mA, wavelength 1.5418 Å). Figure 1(a) shows the XRD patterns for the two samples, LC and MC. In this figure, the points represent the experimental data, and the lines represent the Rietveld [26] fitting using the MAUD [27] program. The XRD pattern of both of the samples show characteristic lines of mixed phase of MoS_2 having hexagonal symmetry ($P6_{3/mmc}$) and β-$Ni(OH)_2$ having a trigonal symmetry ($P\bar{3}m_1$). All the peaks are matched with JCPDS card no: 14-0117 for β-$Ni(OH)_2$ phase and 24-0513 for MoS_2 phase. The extracted parameters viz. lattice constants, crystallite size, root-mean-square (RMS). strain, and the phases present are summarized in Table I. From the XRD analysis shown in Table I, it is seen that the lattice parameters "a" for both MoS_2 and $Ni(OH)_2$ are comparable and that the β-$Ni(OH)_2$ layer is grown on MoS_2 surface along (100) direction. However, a contraction in

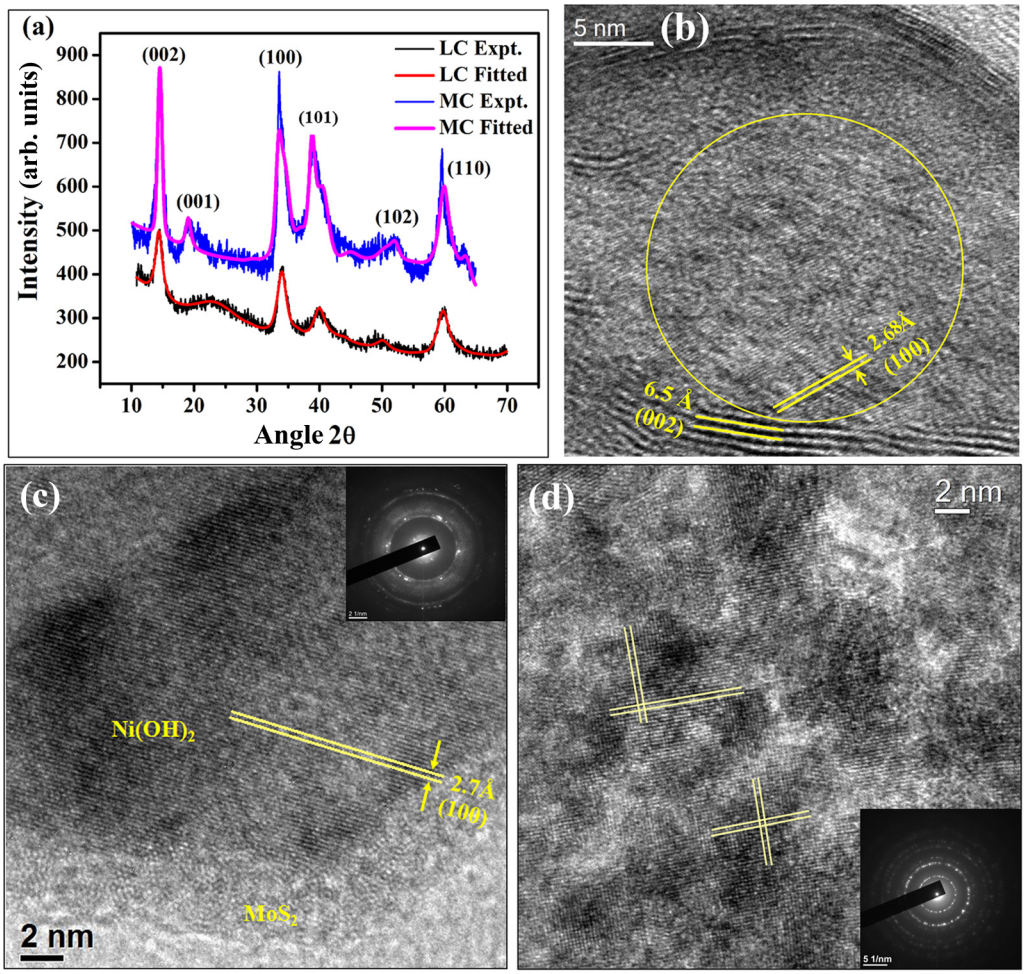

FIG. 1. The XRD and TEM structural characterization of the as-grown $MoS_2/Ni(OH)_2$ composites. (a) The XRD patterns for LC and MC, respectively. Broad line represents the experimental, and narrow line is the curve obtained from Rietveld analysis. (b) Overall growth structure for a typical sample on MoS_2 with interlayer separation 6.5 Å for (002) plane and in plane (100) planes. (c) High resolution lattice image of uniform crystalline phase of $Ni(OH)_2$ with (100) planes having separation of 2.7 Å and MoS_2 in the background for LC. (d) For the sample MC, several randomly oriented (100) planes of $Ni(OH)_2$ are observed.

TABLE I. Parameters obtained after Rietveld analysis of XRD data for samples LC and MC, respectively.

Sample	Phases	Lattice parameters (nm) a	Lattice parameters (nm) c	Crystallite size (nm)	RMS strain $\times 10^{-3}$	Standard deviation
LC	MoS_2	0.311	1.231	7.8	9	1.02
	$Ni(OH)_2$	0.308	0.380	1.22(001)	91	
				15.8(100)	7.6	
				15.8(110)	7.8	
MC	MoS_2	0.307	1.218	32.58	19	1.48
	$Ni(OH)_2$	0.308	0.464	10.9	5.72	

lattice parameter "c" of $Ni(OH)_2$ phase along (001) direction is noticed in thin layered sample (LC) corresponding to a lattice strain $\sim 9.1 \times 10^{-2}$ calculated from Rietveld analysis [26]. A moderate lattice strain of about 7.6×10^{-3} is also obtained among (100) planes. In the case of a comparatively thicker sample (MC), the lattice parameter "c" is close to its bulk value, and, accordingly, the strain drastically decreases to 5.7×10^{-3}. The origin of this huge lattice strain along [001] direction in the thin layer of $Ni(OH)_2$ is due to the interaction of Ni and S at the interface of $Ni(OH)_2$ and MoS_2 as a result of charge transfer from S to Ni. The effect is prominent in the case of sample LC because of a larger distortion of the atoms in each $Ni(OH)_2$ layer due to the above mentioned interaction acting at the interface. In the case of MC, the effect is much less due to stronger binding energy of the atoms present in the interior of the thicker crystalline phase.

Transmission electron microscopy (TEM) of the as-synthesized samples was investigated using a JEOL-2011 high resolution transmission electron microscope to understand the morphology of the growth structures. Figure 1(b) shows the microstructure of as-synthesized layered type MoS_2 with interlayer separation 6.5 Å and in-plane lattice spacing of 2.68 Å [(100) planes]. Due to lattice matching of (100) planes of $Ni(OH)_2$ with lattice spacing 2.7 Å, the epitaxial growth

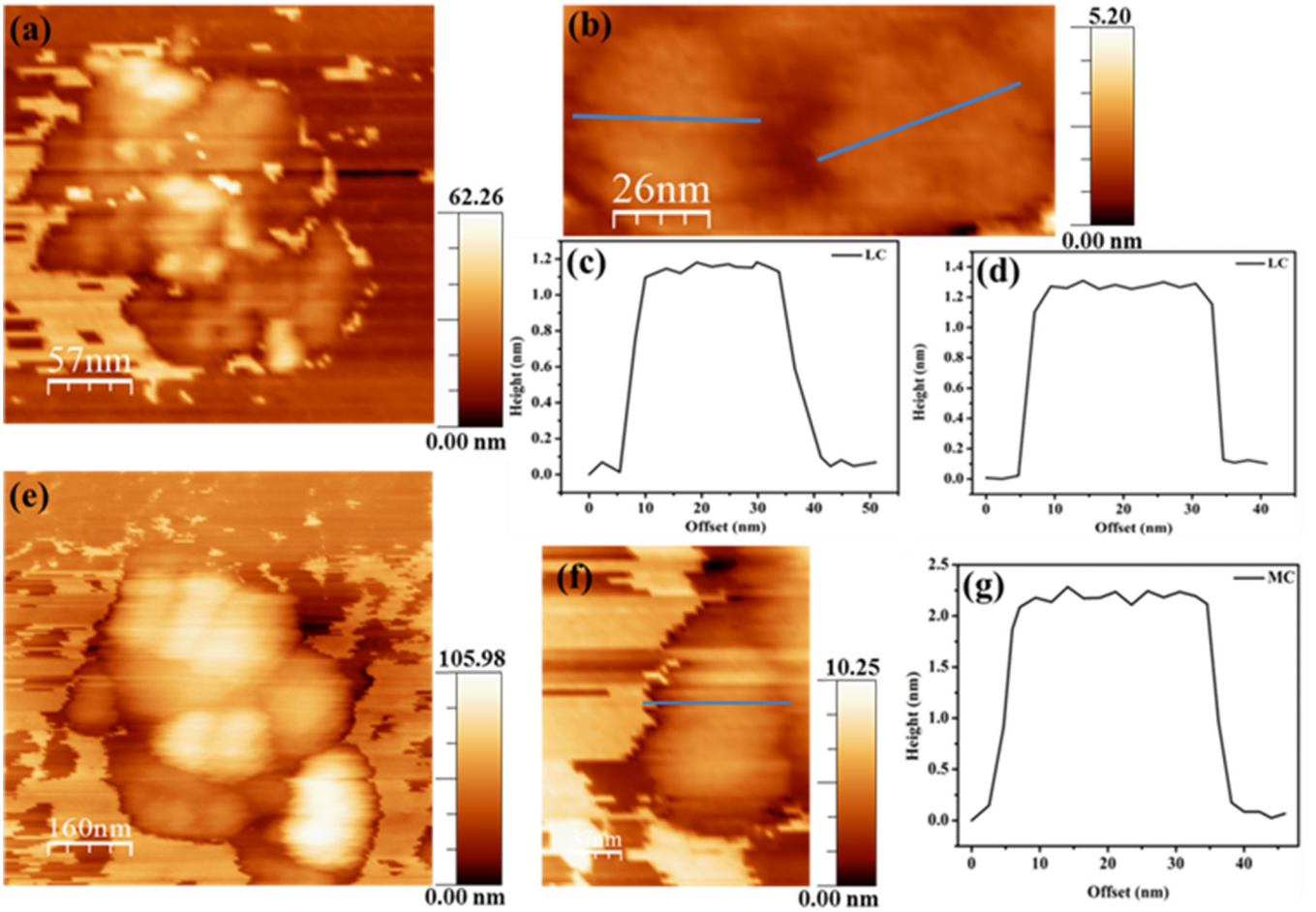

FIG. 2. The AFM images of the $Ni(OH)_2$ layers on MoS_2 surface. (a) Overall image of sample LC. (b) Magnified images. (c), (d) Height profiles for LC. (e) Overall magnified image of MC. (f) Magnified image. (g) Height profile for MC.

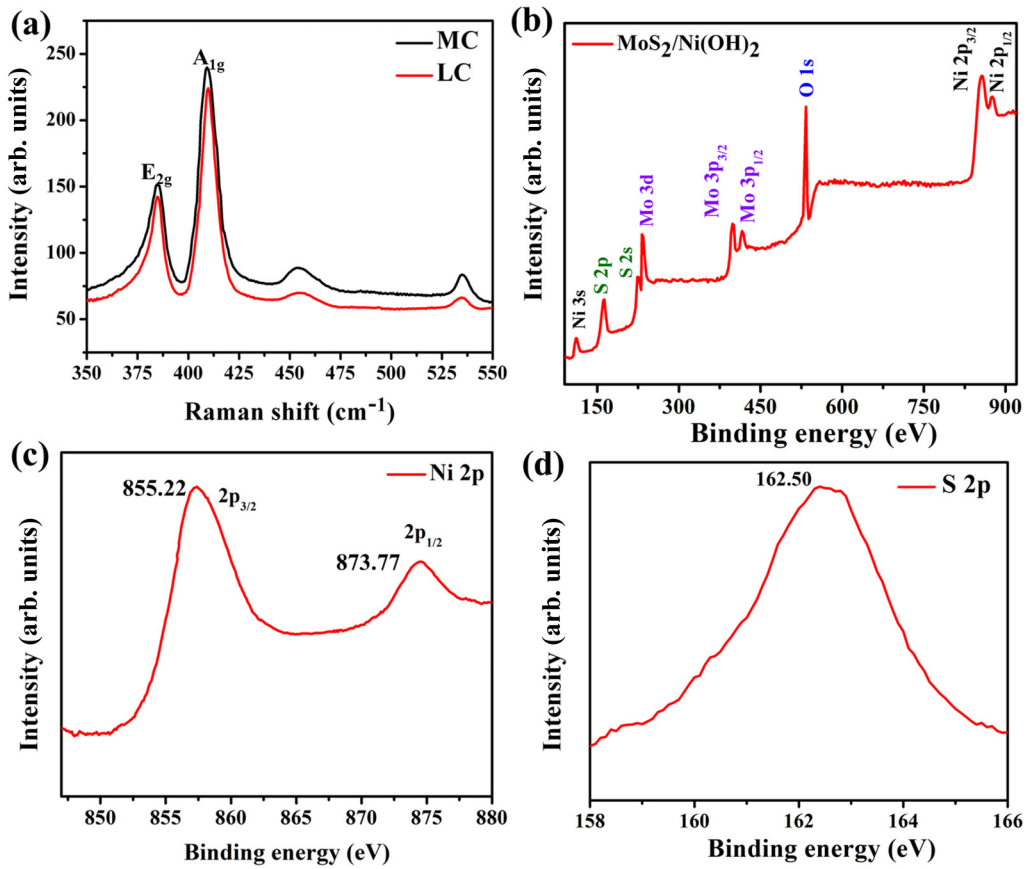

FIG. 3. Raman and XPS analysis. (a) The Raman spectra. (b) The XPS full range view and (c) magnified XPS peaks for Ni $2p$ orbitals and for the (d) S $2p$ orbital.

of the thin layered $Ni(OH)_2$ on MoS_2 surface is observed, as shown in Fig. 1(c). However, because of the lattice strain in the free standing multilayers MoS_2, the as-grown epitaxial $Ni(OH)_2$ layer on MoS_2 surface gets strained, as discussed in the XRD analysis. For MC, due to overgrowth of $Ni(OH)_2$ layers, several randomly oriented (100) planes are observed, as revealed in Fig. 1(d).

B. Atomic force microscopy measurement

In order to measure the thickness of the $Ni(OH)_2$ layers on the MoS_2 surface, we have carried out AFM measurement of the composite material in a Si/SiO_2 wafer. Atomic force microscopy (AFM) is done in the contact mode by PicoLE AFM equipment (Agilent Corp., USA). Figure 2(a) shows the AFM image of the overall $MoS_2/Ni(OH)_2$ composite. $Ni(OH)_2$ layers are grown on MoS_2 surface. The selected portion for the sample LC is magnified in Fig. 2(b). From this, the thickness of the $Ni(OH)_2$ layer for LC is found to be $\sim$1.15 nm and 1.25 nm, as given in Figs. 2(c) and 2(d) with MoS_2 as a background. For MC, the overall image is shown in Fig. 2(e). Selected portion for MC is given in Fig. 2(f). The thickness is 2.25 nm, as obtained from Fig. 2(g). Thus, from AFM measurements, the thickness of the $Ni(OH)_2$ layers, which are grown on the MoS_2 surface, is estimated.

C. Raman and x-ray photoelectron spectroscopy analysis

The x-ray photoelectron spectroscopy (XPS) measurements were carried out using OMICRON-0571 system. Raman spectra are obtained with a micro-Raman (model JYT-6400) system. Raman spectra, shown in Fig. 3(a), exhibit the characteristic features of $Ni(OH)_2$ on MoS_2. Two peaks of MoS_2 appear at 384.7 and 409.2 cm^{-1} for E_{2g} and A_{1g} vibration modes, respectively. Other two broad peaks at 454 and 534.5 cm^{-1} are attributed to the stretching vibrations of Ni–OH and Ni–O modes of $Ni(OH)_2$ phase. From Fig. 3(a), it is seen that the nickel hydroxide peak intensity decreases in case of lower concentrated $Ni(OH)_2$ sample LC.

From the XPS measurement, we get the chemical state of the elements present in the $MoS_2/Ni(OH)_2$ composite and the charge transfer if any from S to Ni at the interface, shown in Fig. 3(b). Three intense peaks at 234, 398.7, and 416.8 eV are observed for Mo $3d$, $3p_{3/2}$, and $3p_{1/2}$, respectively. Another two peaks at 162.5 and 227.3 eV correspond to S $2p$ and $2s$ of MoS_2 phase. Two major peaks with binding energies at 855.22 and 873.77 eV correspond to Ni $2p_{3/2}$ and $2p_{1/2}$ of the $Ni(OH)_2$ phase, as shown in Fig. 3(c). Besides these peaks, the Ni $3s$ peak also appears at 112.9 eV. In addition, the O $1s$ spectrum with a strong peak at 532.4 eV is associated with hydroxide groups (OH^-) of nickel hydroxide. The magnified peak for sulfur $2p$ orbital is shown in Fig. 3(d). For the experimental verification of the charge transfer process from S to Ni, the orbital energies of sulfur and nickel are investigated

TABLE II. Shift in binding energy of the orbitals from XPS analysis.

Elements	Orbital	Experimental binding energy (eV)	Actual binding energy (eV)	Shift in energy (eV) (due to charge transfer)
S	$2p$	162.50	161.80	0.70
Ni	$2p_{3/2}$	855.22	855.90	−0.68

and compared with the pure MoS_2 and $Ni(OH)_2$ phases. The increase in orbital energy of S $2p$ from 161.8 eV to 162.5 eV and decrease in the same for Ni $2p_{3/2}$ from 855.90 eV to 855.22 eV clearly indicates a partial charge transfer from S to Ni at the interface. Table II shows the binding energy values of the orbitals before and after the charge transfer process.

III. RESULTS AND DISCUSSION

A. Magnetic analysis

To investigate the magnetic properties of this thin layered β-$Ni(OH)_2$ grown on the MoS_2 surface, we have carried out magnetic measurements over the temperature range from 2–300 K using a SQUID magnetometer (Quantum design MPMS XL 5). Figure 4(a) shows the field cooled and zero field cooled (FC-ZFC) curves with magnetic field of 50 Oe for both the samples LC and MC. The saturation magnetization at low temperature region and splitting of FC-ZFC curves clearly indicate the ferromagnetic ordering for both the samples LC and MC, although β-$Ni(OH)_2$ is known to be an antiferromagnet in its bulk phase. From the linear fit of the ZFC data as $1/\chi$ plotted as a function of temperature exploiting Curie-Weiss law $\chi = \frac{C}{T-\theta}$ shown in Fig. 4(b), the transition temperature θ and curie constant C are obtained for LC and MC as $\theta = 30$ K, $C = 0.015$ emuK g^{-1}Oe^{-1} and $\theta = 27.2$ K, $C = 0.033$ emuK g^{-1}Oe^{-1}, respectively. Putting the values of C in the equation, $C = \frac{N\mu^2}{3k_B}$, where N is the number of Ni^{2+} spins per gram. The effective magnetic moment μ has been estimated and k_B is the Boltzmann constant. The value of S is calculated for all the samples using equation $\mu^2 = g^2{\mu_B}^2 S(S+1)$, considering the g value (∼2.199), as obtained from electron spin resonance (ESR) spectra given in the inset of Fig. 4(b). The X-band ESR spectra (9.5 GHz) of the sample (solid phase) containing the Ni^{2+} ion in distorted octahedral geometry is done at 300 K. The experiment shows two derivative signals of $S = 1$ species with resonance at

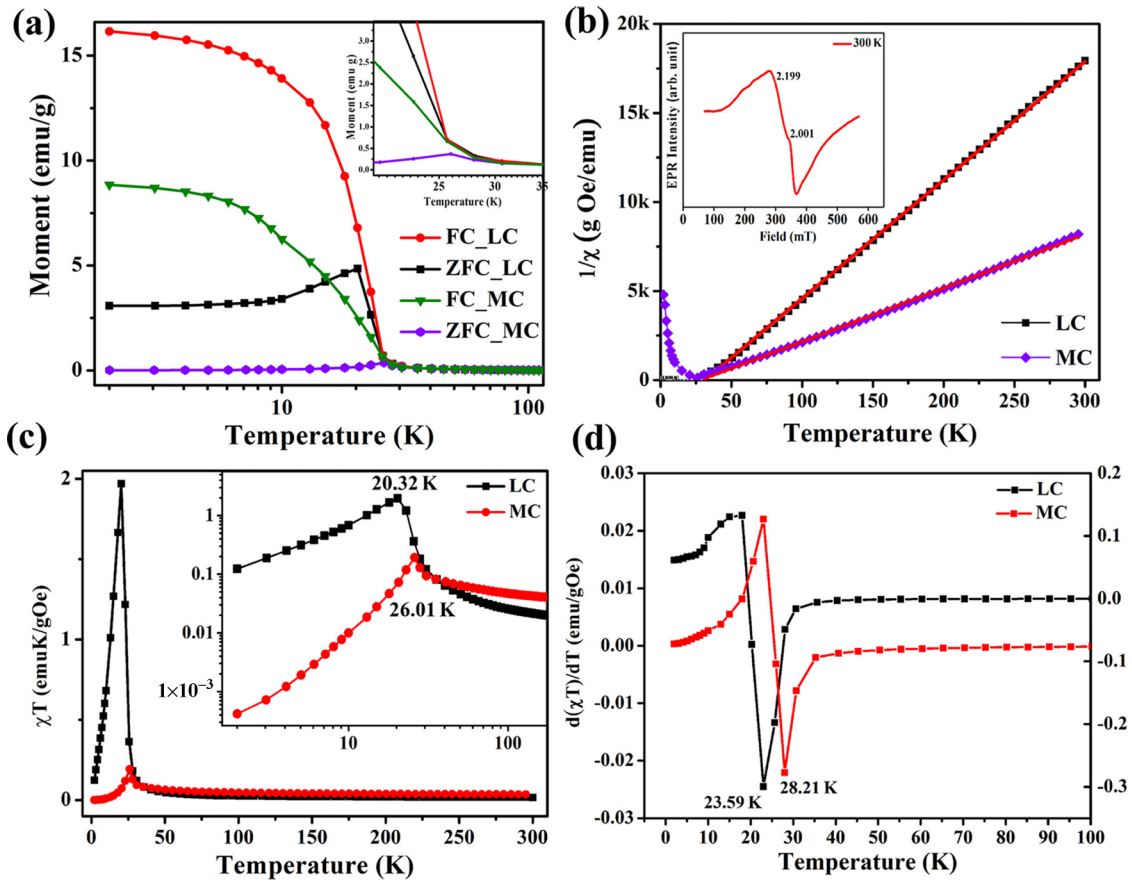

FIG. 4. Magnetization vs temperature curve. (a) The ZFC-FC curves for LC and MC, respectively. Inset shows bifurcation between FC ZFC for the two samples. (b) $1/\chi$ vs T for LC and MC. Red lines represent the curves fitted with Curie-Weiss law. Inset shows the electron paramagnetic resonance (EPR) spectra of a typical sample. (c) χT vs T plot for LC and MC. Insets show the magnified peak positions of the ordering temperatures. (d) Derivative plot of χT for the two samples to show the transition temperatures.

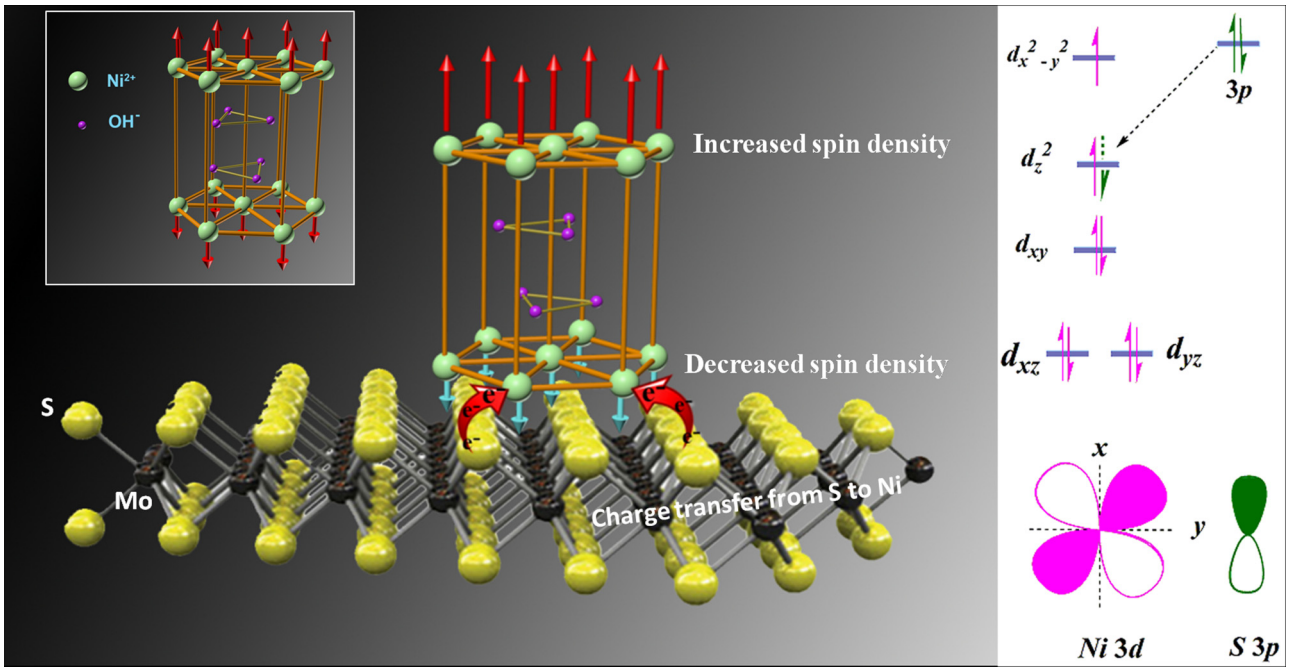

FIG. 5. Change in spin density due to charge transfer at the interface and energy band diagram of S $3p$ and Ni $3d$ orbitals. In the distorted octahedral structure, the splitting is given in the above figure. Fractional charge is transferred from S $3p$ to vacant $3d$ orbital of Ni. As a result, effective magnetic moment is reduced.

$g \approx 2.199$ (g_z) and 2.001 ($g_{x,y}$), as given in the inset of Fig. 4(b). The signal presented a typical axial spectrum, with $g^{\parallel} = 2.199$ and $g^{\perp} = 2.001$, in accordance with the tetragonal distortion of the Ni^{2+} ion. The magnetic susceptibility data are fitted using this experimentally obtained g value for both the samples with $N = 9.33 \times 10^{21}$ for LC and 1.48×10^{22} for MC, respectively. The calculated S values are obtained as 0.86 for LC, whereas for MC the value comes out to be 1.04, which is almost equal to 1. The significant departure from $S = 1$ for Ni^{2+} ion is due to the fractional charge transfer from sulfur $3p$ to nickel $3d$-orbital at the interface to reduce the spin density at the $Ni(OH)_2$ layer adjacent to the MoS_2 surface, resulting in an uncompensated spin moment to the next upper $Ni(OH)_2$ layer, as shown in Fig. 5. $Ni(OH)_2$ has distorted octahedral geometry. Corresponding crystal field splitting is given in the inset of Fig. 5. As the $d_{x^2-y^2}$ state of Ni^{2+} is half filled, electrons are partially transferred from the filled sulfur $3p$ orbitals to Ni $3d$ orbitals and coupled antiferromagnetically with a net reduction of Ni spin, as shown in the energy band diagram. Due to this effect, average spin moment for LC reduces to 0.86 instead of 1. Considering β-$Ni(OH)_2$, a known antiferromagnet with Ni^{2+} spins being antiparallel in the alternate layers, the higher Curie temperature $\theta = 30$ K in the case of LC indicates better ferromagnetic ordering compared to MC in which Curie temperature shifts to lower temperature due to antiferromagnetic upper layers. This is more prominent in the χT vs T plot, as shown in Fig. 4(c). From the inset of Fig. 4(c), strength of antiferromagnetic and ferromagnetic coupling can be understood. For a perfect antiferromagnet, the moment at 0 K should vanish. Here, below the ordering temperature, χT falls off more rapidly for MC than LC, as shown in the inset of Fig. 4(c). At 2 K, the magnitude of χT for MC is 4.17×10^{-4}, and for LC it is 0.12, from which it can be concluded that AFM ordering in the case of MC is much stronger than LC, due to lager fraction of volume ions in the thicker phase. Also, in the case of LC, ferromagnetic ordering is stronger, which is evident from the sharp rising of the χT value as the temperature reaches towards ordering temperature. From the derivative plot of χT vs T, we can clearly determine the transition temperature (T_N), as depicted in Fig. 4(d). Now, differentiating χT with respect to T, we get $\frac{\partial(\chi T)}{\partial T} = -\frac{C\theta}{(T-\theta)^2}$; for positive θ this gives a negative minimum at $T = \theta$, which is because of the FM interaction between the intralayer Ni^{2+} ions, and for negative θ it gives a maximum, which is due to AFM interaction (interlayer coupling). In Fig. 4(d), the dip at the negative side corresponds to FM ordering.

B. Hysteresis curves

The magnetic hysteresis curves for MC and LC at different temperatures are shown in Figs. 6(a) and 6(b). Bulk β-$Ni(OH)_2$ is purely an antiferromagnetic material with Neel temperature at ~26 K due to antiparallel configuration of Ni^{2+} spin moments between the intralayers [19]. Therefore, ferromagnetism with huge coercivity ~2925 Oe in thin layered $Ni(OH)_2$ grown on MoS_2 surface is an interesting observation. To explain this observed ferromagnetic saturation with giant coercivity, we have considered the schematic diagram given in Fig. 5, where antiparallel Ni^{2+} spins are shown in two alternate (001) planes of β-$Ni(OH)_2$ unit cell. Due to charge transfer from S to Ni as indicated, the effective magnetic moment in the layer adjacent to MoS_2 is reduced due to coupling of the transferred charge from the p orbital of sulfur with the unpaired d electrons of Ni resulting uncompensated spins in the next upper layer. For the thin β-$Ni(OH)_2$ layer (LC), the effect of this uncompensated

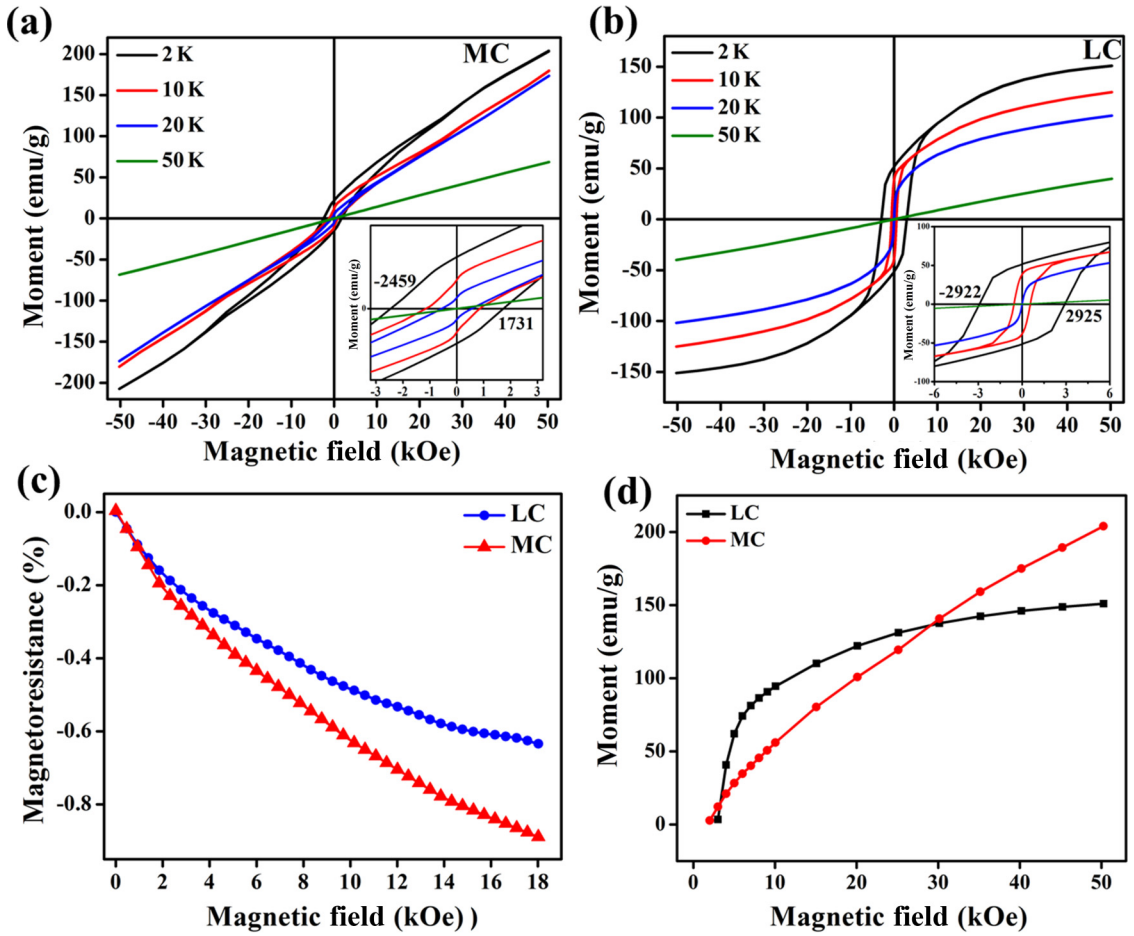

FIG. 6. The M-H loops and magnetoresistance curves (a) and (b) correspond to the hysteresis loop at different temperatures for MC and LC, respectively. Insets show the coercivity values in enlarged view from which a clear exchange bias is seen for sample MC, which is absent for sample LC. (c) Magnetoresistance at room temperature for LC and MC is shown. (d) Comparison of the saturation magnetization for the two cases.

spin at the interface is dominant, giving rise to a ferromagnetic saturation with giant coercivity of about 2925 Oe. It is seen that the coercivity decreases for higher volume fraction of $Ni(OH)_2$ phases as in case of sample MC. The decrease in coercivity with thickness is verified by a further increase in volume fraction of β-$Ni(OH)_2$. The coercivity values at different temperatures are summarized in Table III.

The remarkable enhancement in coercivity in the case of thin layered $Ni(OH)_2$ lies with the strain generated in the film [28–31]. From MAUD analysis, it is seen that $Ni(OH)_2$ layer with the lowest concentration is strained largely along c axis due to the interaction between the two layers as a result of charge transfer from MoS_2 to $Ni(OH)_2$. Because of this effect and high strain induced along the c axis, the surface spins in each layer are pinned, resulting an enhancement in coercivity in thin layered $Ni(OH)_2$ [32,33]. With increasing volume fraction of the hydroxide phase, thickness of the $Ni(OH)_2$ layer increases, and coercivity reduces. This decrease in coercivity with increasing volume fraction arises due to the reduction of strain induced in the layer due to overgrowth along the c axis. From the XRD analysis it is also seen that the lattice strain along the c axis is much lower in the case of MC than in the LC. Figure 6(c) shows the magnetoresistance MR results at room temperature for LC and MC. It is seen that in case of LC, MR is only ~0.6% at 300 K; however for sample MC it changes up to 0.9%. Figure 6(d) is given to compare the saturation magnetization of LC with MC.

TABLE III. Comparison of coercivity values at different temperatures.

Temp.	LC	MC
$T = 2$ K	2925 Oe	1731 Oe
	−2922 Oe	−2459 Oe
$T = 10$ K	559 Oe	864 Oe
	−559 Oe	−1147 Oe
$T = 20$ K	5.36 Oe	561 Oe
	−5.55 Oe	−557 Oe
$T = 50$ K	5.86 Oe	8.54 Oe
	−10.33 Oe	−11.31 Oe

C. Magnetostructural correlation

For a ferromagnetic material at $T \to 0$ K, saturation magnetization is given by $M_s = Ng\mu_B\langle S\rangle$. In the present case for LC, using $g = 2.2$ and $S = 0.86$, the value of M_s comes out

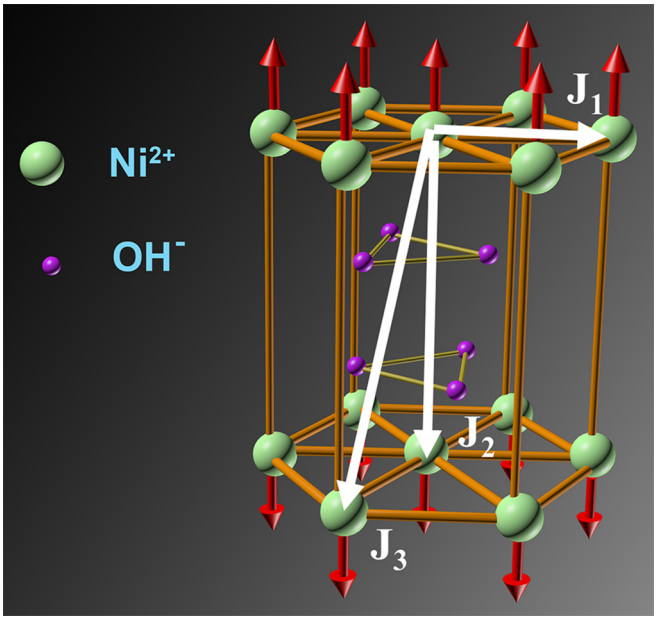

FIG. 7. In-plane and interplane exchange coupling between the Ni^{2+} ions in the intralayer and interlayers. J_1 represents FM coupling and J_2, J_3 for AFM coupling.

to be 163.6 emu g^{-1}, which is comparable to the experimental value of 150 emu g^{-1}. In order to find the strength of coupling between the Ni^{2+} ions present in LC and MC, we have used a two-sublattice model [34] using a molecular field approach, and the standard Hamiltonian can be written as

$$\mathcal{H} = -2\sum_{i,j} J_{ij}\,\vec{S_i}.\vec{S_j} - g\mu_B\vec{H}.\sum_i \vec{S_i}. \qquad (1)$$

Here, we assume an Ising type of ordering, and considering the magnetic field parallel to the c axis, the three exchange coupling constants J_1, J_2, and J_3 shown in Fig. 7 can be expressed by the following equations:

$$3k_B\theta = 2S(S+1)[J_1Z_1 + J_2Z_2 + J_3Z_3] \qquad (2)$$

$$3k_BT_N = 2S(S+1)[J_1Z_1 - J_2Z_2 - J_3Z_3], \qquad (3)$$

where k_B is the Boltzmann constant, $Z_1 = 6$, $Z_2 = 2$, and $Z_3 = 12$ are the number of nearest neighbors taking part in the interactions considering the unit cell as given in Fig. 7. J_1, J_2, and J_3 are the exchange coupling constants whose magnitude and sign determine the nature of interaction between the Ni^{2+} ions. Out of these three exchange constants, the most important one is the first in-plane nearest neighbor J_1. After that, the next important one is the first out-of-plane nearest neighbor J_2, which couples the spins of different hexagonal planes. Without J_2, there will be no three-dimensional ordering in the system, and J_3 is the second out-of-plane neighbor. For sample LC, we take $\theta = 30$ K, as obtained from the Curie-Weiss fitting and $T_N = 23.59$ K, taken from the derivative plot of χT. Using these values and $S = 0.86$ for LC, from Eqs. (2) and (3) we find $J_1/k_B = 4.20$ K, $J_2/k_B = 0.50$ K and $J_3/k_B = 0.17$ K. Similarly in the case of sample MC using $\theta = 27.2$ K and $T_N = 28.2$ K, the values of the exchange constants are estimated as $J_1/k_B = 3.25$ K, $J_2/k_B = -0.047$ K and $J_3/k_B = -0.015$ K. In the earlier studies, the values of exchange parameters for bulk β-$Ni(OH)_2$ were reported as $J_1/k_B = 2.70$ K, $J_2/k_B = -0.28$ K and $J_3/k_B = -0.09$ K [35]. Note that the magnitude of exchange constant J_1 in our cases is larger than the bulk β-$Ni(OH)_2$ phase. As J_1 designates ferromagnetic ordering in the system, in our case the strength of FM coupling is stronger than the bulk phase stated earlier. Therefore, from the sign and magnitude of the exchange constants of the two samples, it is seen that the interlayer coupling for MC is antiferromagnetic; however, for LC the coupling is ferromagnetic. This transition from antiferromagnetic to ferromagnetic in the case of LC is due to the charge transfer effect from MoS_2 to adjacent $Ni(OH)_2$ layer as well as to the strain induced ferromagnetism along the c axis. Appearance of such strain induced ferromagnetism in antiferromagnetic thin layers is also reported earlier by several others [36–39]. The effects are much more pronounced in the case of LC than MC, resulting in positive values of exchange constants J_2 and J_3 for LC. This indicates that the dominant exchange interaction is FM, while negative J_2 and J_3 for MC depict the AFM interaction among the interlayers. In addition to these effects, the observed enhanced magnetic response may also arise due to uncompensated surface spins from an odd number of $Ni(OH)_2$ layers.

D. Temperature dependent magnetotransport

To investigate the role of charge transfer at the MoS_2/$Ni(OH)_2$ interface on magnetoconductivity, we have measured conductivity for all the three samples as a function of temperature (3–300 K) with and without magnetic field, as shown in Fig. 8(a) for LC and MC, respectively. For resistivity measurements, we have used a Keithley 2601A SourceMeter and a Keithley 2182A nanovoltmeter using a standard four probe method. For low temperature setup, the Janis closed cycle cryostat has been used. All the measurements were done under vacuum (10^{-7} bar) using a Hind High Vacuum pumping system. The corresponding change in magnetoconductivity $\Delta\sigma = [\sigma(H)\text{-}\sigma(0)]$ with temperature is depicted in Fig. 8(b) from which it is seen that for all samples $\Delta\sigma$ increases with temperature, which is unusual to the existing literature because of the increasing scattering rate with temperature [40,41]. To explain this observed magnetoconductivity behavior, we have considered temperature dependent Rashba spin-orbit coupling due to charge sharing at the MoS_2/$Ni(OH)_2$ interface. Rashba type spin-orbit coupling is mainly observed in 2D semiconductor systems where there is a natural interface asymmetry in heterostructures that is significantly affected by the electric fields acting normal to the surface [42]. In this case, due to charge transfer from S $3p$ to Ni $3d$ at the interface, a potential barrier is formed as a result of d-p mixing [43], and the electric field associated with this charge transfer acts perpendicularly to the 2D surface. Now the Rashba spin-orbit coupling acting at the interface is affected by this internal electric field. In order to understand the interplay of Rashba spin-orbit coupling (SOC) with the Landé g factor, we have considered the Hamiltonian of an electron in the presence of an external magnetic field, which is mostly consisting of two parts. One is a normal Zeeman term, and the other is a spin-orbit interaction term (H_{so}).

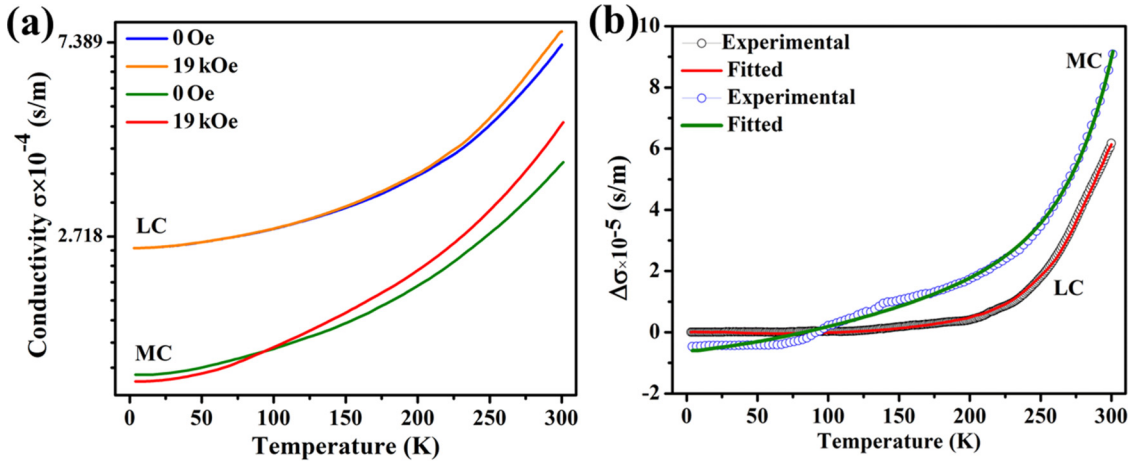

FIG. 8. Magnetotransport curves. (a) Conductivity as a function of temperature for LC and MC with and without magnetic fields. (b) Corresponding change in magnetoconductivity for LC and MC, respectively. Solid curve is from conductivity fitted with Eq. (6).

The H_{so} is basically written in terms of a Rashba spin-orbit coefficient α, which is a function of a g factor [44]. The α determines the strength of spin-orbit coupling. Thus, in spin-orbit interaction, the g factor is introduced through this α term in the Hamiltonian. Rashba SOC produces the dominant effect on the variation of the g factor, and it is significantly affected by the electric field. The coefficient of spin-orbit coupling α as a function of g as expressed by others [45,46] is given by

$$\alpha = g(g-1)\frac{\pi e\hbar^2\varepsilon}{4m_*^2c^2}, \tag{4}$$

where g is the Landé g factor, ε is the asymmetric structure induced electric field, c is the speed of light, and m_* is the effective mass of the electron. Temperature dependence in spin-orbit coupling has been introduced through the Landé g factor in many experiments [22–25], indicating linear temperature dependence in g. This can be understood from the definition of the electron g-factor in the presence of a magnetic field that is proportional to the energy difference of band splitting ΔE, which is of fundamental temperature dependence [47]. In a semiconducting system, the band gap generally decreases with increasing temperature due to lattice expansion, which causes a decrease in the g factor [45]. Therefore, the coefficient of spin-orbit coupling α can be modified using the linear temperature dependence of g ($g = g_0 - \lambda T$). Substituting this into Eq. (4), we get the modified expression for α as

$$\alpha = [g_0(g_0-1) - (2g_0-1)\lambda\mathrm{T}+\lambda^2\mathrm{T}^2]\frac{\pi e\hbar^2\varepsilon}{4m_*^2c^2}. \tag{5}$$

The fractional charge transfer from S $3p$ to Ni $3d$ orbital of the $MoS_2/Ni(OH)_2$ composite creates a potential barrier at the interface. This is called d-p mixing, and it is well known in the literature [43]. This electric field at the junction interacts with the conduction electron via SOC, and conductivity is modified due to the presence of this electric field. With increasing temperature, charge transfer at the interface is decreased, and as a result, interaction between the conduction electron and transferred charges is destroyed, resulting in a decrease in SOC. Justification behind this reduction in spin-orbit coupling with temperature lies with the temperature dependent charge sharing (d-p mixing) at the interface, which becomes weaker due to thermal energy as temperature rises. At very low temperature, there is a better charge transfer, and this reduces as the temperature rises at room temperature.

In order to explain the temperature dependent change in magnetoconductivity $\Delta\sigma$, we have considered electron-electron interaction and temperature dependent spin-orbit coupling being operative at the interface [48]. Based on this localization interaction model, the overall conductivity can be written as a sum of these two contributions,

$$\Delta\sigma = \sigma_0 + aT^{1/2} + bT^{[g_0(g_0-1)-(2g_0-1)\lambda T+\lambda^2T^2]}, \tag{6}$$

where the first term (σ_0) is the zero temperature contribution of conductivity due to localization effects, the second term represents the electron-electron interaction term $T^{1/2}$, the third term is the temperature dependent spin-orbit term, and a, b, λ, and g_0 are the parameters. The experimental change in magnetoconductivity $\Delta\sigma$ in Fig. 8(b) is fitted with Eq. (6) using σ_0, a, b, g_0, and λ as parameters. The solid lines represent the theoretical curves, as obtained from Eq. 6, and the points are experimental data. It is seen that the data are well fitted by Eq. (6), and the values of the parameters extracted from the fitting procedure are summarized in Table IV. Here electron-electron interaction dominates at the low temperature region; the negative values of σ_0 for all of the samples indicate the dominant role of electron-electron interaction in contributing magnetoconductivity. The value of g_0 is the lowest for LC, which indicates the best coupling due to greater charge transfer at the $MoS_2/Ni(OH)_2$ interface. For MC, coupling decreases due to increasing thickness of the $Ni(OH)_2$ phase, and accordingly g_0 increases. This is listed in Table IV.

We have also measured magnetoconductance as a function of increasing magnetic field at different temperatures down to 4 K in order to verify the field dependence on

TABLE IV. Parameters obtained after fitting the experimental data with Eq. 6.

	LC		MC	
Parameters	Value	Standard error	Value	Standard error
σ_0	-3.630×10^{-6}	2.408×10^{-7}	-3.841×10^{-5}	3.620×10^{-7}
a	1.519×10^{-8}	2.470×10^{-9}	3.044×10^{-6}	2.883×10^{-7}
b	8.195×10^{-6}	2.021×10^{-6}	3.086×10^{-5}	1.901×10^{-6}
g_0	0.5423	0.0699	0.8821	0.0500
λ	0.0027	1.390×10^{-4}	0.0034	1.400×10^{-4}

magnetotransport. As depicted in Figs. 9(a) and 9(b), for MC, magnetoconductance is positive at the high temperature region, and at the low temperature it is negative. Hence, there is a transition from positive to negative magnetoconductance at a temperature near about 80 K for MC. In the case of LC, no such transition is found, and magnetoconductance is positive throughout the entire temperature range down to 4 K. These two results are also consistent with the $\Delta\sigma$ vs T plots, as discussed above where a transition in $\Delta\sigma$ was found for MC. At lower temperature, the dominant *e-e* interaction is responsible for this negative magnetoconductance behavior, and at high temperature weak spin-orbit coupling is active to give rise to positive magnetoconductance. Thus, the field dependency is also in agreement with the temperature dependent magnetoconductivity ($\Delta\sigma$), which shows a transition with temperature.

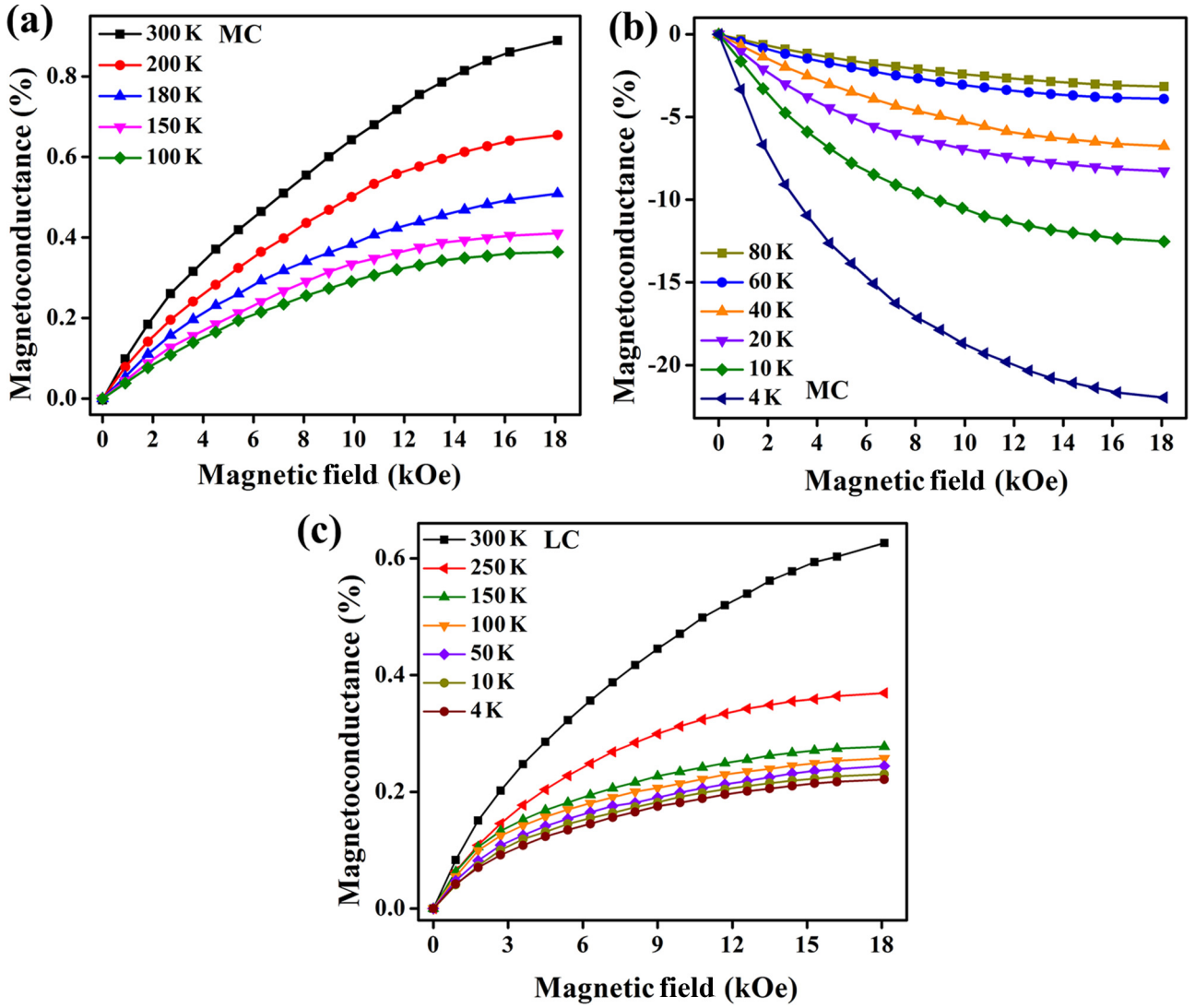

FIG. 9. Magnetoconductivity as a function of magnetic field. (a), (b) For sample MC, where there is a transition from positive to negative at low temperature. (c) For sample LC, positive change over all of the temperature range.

IV. CONCLUSION

In summary, an ultrathin layer of $Ni(OH)_2$ is grown on the MoS_2 surface. Instead of antiferromagnetism being operated in the bulk phase, the thin layer of $Ni(OH)_2$ shows ferromagnetic ordering with giant coercivity. The charge transfer from S to Ni at the $MoS_2/Ni(OH)_2$ interface results in a d-p mixing, which causes uncompensated spins at the $Ni(OH)_2$ layer adjacent to MoS_2 surface, giving rise to ferromagnetic ordering. The unusual magnetoconductivity is explained by the temperature dependent spin-orbit coupling acting at the interface. The use of the antiferromagnetic thin layer to become ferromagnetic with a wide range of coercivity values due to charge transfer effect is a new concept and will be useful in fabricating magnetic contacts of MoS_2 based spin transistors.

ACKNOWLEDGMENTS

S.B., D.D., and B.K.S. acknowledge Department of Science and Technology (DST)-INSPIRE, Council of Scientific & Industrial Research (CSIR)-SPM, and CSIR, New Delhi, respectively, for awarding their fellowships. S.K.S. acknowledges DST, New Delhi, Government of India for financial support of Project No. SR/NM/NS-1089/2011.

[1] A. K. Geim and I. V. Grigorieva, Nature **499**, 419 (2013).
[2] K. S. Novoselov, V. Fal, and L. Colombo, Nature **490**, 192 (2012).
[3] A. J. Akhtar, A. Gupta, B. K. Shaw, and S. K. Saha, Appl. Phys. Lett. **103**, 242902 (2013).
[4] M. Baskey and S. K. Saha, Adv. Mater. **24**, 1589 (2012).
[5] B. Dlubak, M. B. Martin, C. Deranlot, B. Servet, S. Xavier, R. Mattana, M. Sprinkle, C. Berger, W. A. De Heer, and F. Petroff, Nature Physics **8**, 557 (2012).
[6] S. K. Saha, M. Baskey, and D. Majumdar, Adv. Mater. **22**, 5531 (2010).
[7] K. F. Mak, C. Lee, J. Hone, J. Shan, and T. F. Heinz, Phys. Rev. Lett. **105**, 136805 (2010).
[8] B. Radisavljevic, A. Radenovic, J. Brivio, V. Giacometti, and A. Kis, Nat. Nanotech. **6**, 147 (2011).
[9] K. F. Mak, K. He, J. Shan, and T. F. Heinz, Nat. Nanotech. **7**, 494 (2012).
[10] S. Das, H. Y. Chen, A. V. Penumatcha, and J. Penumatcha, Nano Lett. **13**, 100 (2013).
[11] J. R. Chen, P. M. P. Odenthal, A. Swartz, G. C. Floyd, H. Wen, K. Y. Luo, and R. K. Kawakami, Nano Lett. **13**, 3106 (2013).
[12] R. Jansen and B. C. Min, Phys. Rev. Lett. **99**, 246604 (2007).
[13] X. Liu, C. Z. Wang, Y. X. Yao, W. C. Lu, M. Hupalo, M. C. Tringides, and K. M. Ho, Phys. Rev. B **83**, 235411 (2011).
[14] S. Mandal and S. K. Saha, Appl. Phys. Lett. **105**, 022402 (2014).
[15] K. Pi, K. M. McCreary, W. Bao, W. Han, Y. F. Chiang, Y. Li, S. W. Tsai, C. N. Lau, and R. K. Kawakami, Phys. Rev. B **80**, 075406 (2009).
[16] S. Sahoo, T. Kontos, J. Furer, C. Hoffmann, M. Gräber, A. Cottet, and C. Schönenberger, Nature Physics **1**, 99 (2005).
[17] A. Avsar, T. Y. Yang, S. Bae, J. Balakrishnan, F. Volmer, M. Jaiswal, and B. Ozyilmaz, Nano Lett. **11**, 2363 (2011).
[18] Y. G. Semenov, K. W. Kim, and J. M. Zavada, App. Phys. Lett. **91**, 153105 (2007).
[19] J. D. Rall, M. S. Seehra, and E. S. Choi, Phys. Rev. B **82**, 184403 (2010).
[20] J. D. Rall, M. S. Seehra, N. Shah, and G. P. Huffman, J. Appl. Phys. **107**, 09B511 (2010).
[21] S. D. Tiwari and K. P. Rajeev, Phys. Rev. B **77**, 224430 (2008).
[22] K. Iwahana, K. Tara, and H. Ohkura, Solid State Commun. **42**, 19 (1982).
[23] M. Motyka, F. Janiak, G. Sek, J. Misiewicz, and K. D. Moiseev, Appl. Phys. Lett. **100**, 211906 (2012).
[24] M. H. Liu, J. Bundesmann, and K. Richter, Phys. Rev. B **85**, 085406 (2012).
[25] M. Kim and B. I. Min, Phys. Rev. B **89**, 121106(R) (2014).
[26] H. M. Rietveld, J. Appl. Cryst. **2**, 65 (1969).
[27] L. Lutterotti, MAUD 2002, version 1 85.
[28] Y. Hua, Z. Wangy, S. Lizhu, Z. Muyu, W. Jianping, and L. Helie, J. Phys. D: Appl. Phys. **29**, 2574 (1996).
[29] N. Anuniwat, M. Ding, S. J. Poon, S. A. Wolf, and J. Lu, J. Appl. Phys. **113**, 043905 (2013).
[30] B. H. Liu and J. Ding, Appl. Phys. Lett. **88**, 042506 (2006).
[31] Y. C. Wang, J. Yi. Ding, J. Liu, B. H. Yu, and Z. X. Shen, Appl. Phys. Lett. **84**, 2596 (2004).
[32] H. D. Chopra, D. X. Yang, P. J. Chen, D. C. Parks, and W. F. Egelhoff, Phys. Rev. B **61**, 9642 (2000).
[33] H. Ohldag, A. Scholl, F. Nolting, E. Arenholz, S. Maat, A. T. Young, M. Carey and J. Stöhr, Phys. Rev. Lett. **91**, 017203 (2003).
[34] A. H. Morrish, *The Physical Principles of Magnetism*, edited by A. H. Morrish (IEEE Press, New York, 2001), p. 447.
[35] T. Enoki and I. Tsujikawa, J. Phys. Soc. Jpn. **39**, 317 (1975); **45**, 1515 (1978).
[36] J. S. White, M. Bator, Y. Hu, H. Luetkens, J. Stahn, S. Capelli, S. Das, M. Döbeli, Th. Lippert, V. K. Malik, J. Martynczuk, A. Wokaun, M. Kenzelmann, Ch. Niedermayer, and C. W. Schneider, Phys. Rev. Lett. **111**, 037201 (2013).
[37] F. Rivadulla, Z. Bi, E. Bauer, B. Rivas-Murias, and J.Quanxi, Chem. Mater. **25**, 55 (2013).
[38] Z. K. Tang, W. Liu, D.-Y. Zhang, W.-M. Lau, and L.-M. Liu, RSC Adv. **5**, 77154 (2015).
[39] X. J. Liu, C. Song, F. Zeng, F. Pan, B. He, and W. S. Yan, J. App. Phys. **103**, 093911 (2008).
[40] C. H. Shang, J. Nowak, R. Jansen, and J. S. Moodera, Phys. Rev. B **58**, R2917(R) (1998).
[41] A. CarIşin and R. V. Coleman, Phys. Rev. **142**, 372 (1966).
[42] P. S. Eldridge, W. J. H. Leyland, P. G. Lagoudakis, O. Z. Karimov, M. Henini, D. Taylor, R. T. Phillips, and R. T. Harley, Phys. Rev. B **77**, 125344 (2008).
[43] A. J. Akhtar, A. Gupta, D. Chakravorty, and S. K. Saha, AIP Advances **3**, 072124 (2013).
[44] S. Prabhakar, J. E. Raynolds, and R. Melnik, Phys. Rev. B **84**, 155208 (2011).
[45] L. Zhang, Y. B. Chen, B. Zhang, J. Zhou, S. Zhang, Z. Gu, S. Yao, and Y. Chen, J. Phys. Soc. Jpn. **83**, 054707 (2014).
[46] S. Bandyopadhyay and M. Cahay, *Introduction to Spintronics* (CRC Press, Boca Raton, Florida, 2008).
[47] M. Oestreich and W. W. Ruhle, Phys. Rev. Lett. **74**, 2315 (1995).
[48] P. A. Lee and T. V. Ramakrishnan, Rev. Mod. Phys. **57**, 287 (1985).